Real-Time Probing of Membrane Transport in Living Microbial Cells Using Single Nanoparticle Optics and Living Cell Imaging†

Xiao-Hong Nancy Xu,* William J. Brownlow, Sophia V. Kyriacou, Qian Wan, and Joshua J. Viola

Department of Chemistry and Biochemistry, Old Dominion University, Norfolk, Virginia 23529

Received December 12, 2003; Revised Manuscript Received June 8, 2004

ABSTRACT: Membrane transport plays a leading role in a wide spectrum of cellular and subcellular pathways, including multidrug resistance (MDR), cellular signaling, and cell−cell communication. *Pseudomonas aeruginosa* is renowned for its intriguing membrane transport mechanisms, such as the interplay of membrane permeability and extrusion machinery, leading to selective accumulation of specific intracellular substances and MDR. Despite extensive studies, the mechanisms of membrane transport in living microbial cells remain incompletely understood. In this study, we directly measure real-time change of membrane permeability and pore sizes of *P. aeruginosa* at the nanometer scale using the intrinsic color index (surface plasmon resonance spectra) of silver (Ag) nanoparticles as the nanometer size index probes. The results show that Ag nanoparticles with sizes ranging up to 80 nm are accumulated in living microbial cells, demonstrating that these Ag nanoparticles transport through the inner and outer membrane of the cells. In addition, a greater number of larger intracellular Ag nanoparticles are observed in the cells as chloramphenicol concentration increases, suggesting that chloramphenicol increases membrane permeability and porosity. Furthermore, studies of mutants (nalB-1 and ΔABM) show that the accumulation rate of intracellular Ag nanoparticles depends on the expression level of the extrusion pump (MexAB−OprM), suggesting that the extrusion pump plays an important role in controlling the accumulation of Ag nanoparticles in living cells. Moreover, the accumulation kinetics measured by Ag nanoparticles are similar to those measured using a small fluorescent molecule (EtBr), eliminating the possibility of steric and size effects of Ag nanoparticle probes. Susceptibility measurements also suggest that a low concentration of Ag nanoparticles (1.3 pM) does not create significant toxicity for the cells, further validating that single Ag nanoparticles (1.3 pM) can be used as biocompatible nanoprobes for the study of membrane transport kinetics in living microbial cells.

All living organisms appear to be equipped with unique membrane transport apparatuses that protect the cells from hazardous and noxious compounds (*1*−*3*). Membrane permeability and active extrusion systems in many living organisms, such as bacteria, yeast, molds, and mammalian cells, play a crucial role in controlling the accumulation of specific intracellular substances, leading to the cellular self-defense mechanism that can resist incoming noxious compounds (*1*−*4*). Microbial cells, however, have membrane transport mechanisms that are substantially distinguished from those in mammalian cells. For example, current evidence shows that endocytosis, pinocytosis, and exocytosis do not exist in microbial cells (prokaryotes), whereas these processes are widely observed in mammalian cells (eukaryotes).

Pseudomonas (P.)[1] *aeruginosa* is selected for this study because *P. aeruginosa* is a ubiquitous Gram-negative bacterium and has emerged as a major opportunistic human pathogen and the leading cause of nosocomial infections in cancer, transplant, burn, and cystic fibrosis patients (*1*−*3*). These infections are impossible to eradicate due in part to the bacterium's intrinsic resistance to a wide spectrum of structurally and functionally unrelated antibiotics (*1*−*6*).

Several multi-drug efflux systems including MexAB−OprM, MexCD−OprJ, MexEF−OprN, and MexXY−OprM have been reported in *P. aeruginosa* (*7*−*10*). The MexAB−OprM system is the major efflux pump in wild-type (WT) *P. aeruginosa*. This pump consists of two inner membrane proteins (MexA and MexB) and one outer membrane protein (OprM) (*7, 8*). The pump is believed to selectively extrude antibiotics using a proton motive force as an energy source (*2, 7*). Several studies have described the interplay between the MexAB−OprM efflux system and the outer membrane barrier, leading to multi-drug resistance (MDR) (*11*−*14*). However, such membrane transport mechanisms remain incompletely understood.

The primary methods for the study of bacterial extrusion (resistance) mechanisms measure the accumulation of

† This work is supported in part by NIH (RR15057-01), Old Dominion University, in the form of start-up fund and a Dominion Scholar Fellowship (Q. W.), and the Amideast Scholarship and Starr Foundation Scholarship (S. V. K.).

* To whom correspondence should be addressed. Email: xhxu@odu.edu. Web site: www.odu.edu/sci/xu/xu.htm; Tel/fax: (757) 683-5698.

[1] Abbreviations: Ag: silver; AZT, aztreonam; EtBr, ethidium bromide; MDR, multi-drug resistance; MIC, minimum inhibitory concentration; ms, millisecond; nm, nanometer; OD, optical density; *P, Pseudomonas*; LSPRS, localized surface plasmon resonance spectra; TEM, transmission electron microscope; WT, wide-type.

10.1021/bi036231a CCC: $27.50
Published on Web 07/24/2004

quinolone antibiotics in bacteria using radioactively labeled (^{14}C and ^{3}H) quinolones, or natural fluorescent quinolones. A review article of these methods has been published (*15*). Given that a common characteristic of MDR of bacteria (*P. aeruginosa*) is their broad resistance to quinolones, the popular method for assessing MDR measures time-dependent fluorescence intensity of quinolones in bulk bacterial cells (*15*−*18*). Fluorescent quinolones, such as ethidium bromide (EtBr), are particularly suitable to be used as a probe for the study of the MDR mechanism because these quinolones emit weak fluorescence in aqueous solution (outside cells) and become strongly fluorescent in nonpolar and hydrophobic environments, especially as the quinolone molecules enter cells and intercalate with DNA. Thus, the time-dependent fluorescence intensity of quinolones (e.g., EtBr) has been widely used for real-time monitoring of the accumulation of substrates in bulk bacterial cells (*15*−*18*). This approach provides the sum of accumulation kinetics obtained from a large population of cells. Individual cells, however, act independently and have unsynchronized membrane permeability, efflux, and accumulation kinetics (*18*, *19*). Therefore, the accumulation kinetics of individual cells is lost in bulk measurements. Furthermore, the bulk measurement using time-dependent fluorescence intensity cannot provide insights into the change of membrane permeability and pore sizes in single living cells. Thus, bulk measurements are unable to address several important questions, such as when, where, and how the substrates induce the change of membrane pore size, membrane permeability, and efflux machinery, leading to the MDR.

Currently, the sizes of membrane pores rely upon X-ray crystallography measurements, which are limited by the difficulties of crystallization of membrane proteins and are unable to provide real-time kinetic information about the sizes of membrane pores in living cells. Recently, staining assays have been used to study the MDR in eukaryotic cells using fluorescence microscopy (*20*, *21*). Unfortunately, these techniques are quite often applied with cell fixation and high concentration of fluorescence dyes that frequently lead to cell death. Consequently, the fluorescent staining assays for the dead-cell imaging are unable to offer real-time kinetic information for membrane transport in living cells. Because the current techniques cannot measure real-time change of membrane pores at nanometer resolution, many questions in regard to membrane transport in living cells remain unanswered (*1*, *6*). For example, what size of substrates can be transported through the inner and outer membranes of living microbial cells? Do the membrane-transport kinetics depend on the sizes of substrates? Do substrates induce the change of membrane permeability and pore sizes, activate, or accelerate, the extrusion mechanism of the cells (so-called inductive mechanism), leading to MDR? These are the key questions to be addressed in order to fully understand the membrane transport and MDR mechanism.

To address some of these questions, we have developed a new tool that uses silver (Ag) nanoparticles as nanometer probes to determine the sizes of substrates that can be transported through the membrane of living microbial cells and to measure accumulation kinetics of the substrates in real time at the single-cell resolution (*22*). The challenges of such a study include (i) how to overcome the rapid motion of tiny bacterial cells with a size of $2 \times 0.5 \times 0.5$ μm in suspension so that the living cells can be confined and continuously monitored in suspension for hours, (ii) how to simultaneously monitor a group of individual cells so that one can obtain statistical information on bulk cells at the single-cell resolution, and (iii) how to develop a new imaging tool that can measure the nanometer probes moving in and out of living cells for real-time monitoring of the change of membrane permeability and efflux kinetics at the nanometer (nm) resolution.

We have overcome these challenges. We have developed and applied a microchannel system to confine living bacterial cells in suspension with no need to immobilize them, which allows living bacterial cells to be continuously monitored for hours (*18*, *23*). We have simultaneously imaged bulk living cells at the single-cell resolution using a CCD camera coupled with a dark-field optical microscope. We have developed Ag nanoparticles as nanometer probes to directly image the changes of membrane pore sizes and permeability at the nanometer (nm) and millisecond (ms) resolution using optical microscopy (*22*, *24*). The quantum yield of Rayleigh scattering of 20 nm of Ag nanoparticles is about seven orders of magnitude higher than the fluorescent quantum yield of a single fluorescence dye molecule (R6G). In addition, the scattering intensity of Ag nanoparticles increases proportionally as the volume of nanoparticles increases. Furthermore, unlike fluorescence dyes, Ag nanoparticles are resistant to photobleaching. Therefore, these Ag nanoparticles are extremely bright under the dark-field microscope and can be used for real-time monitoring of membrane transport in living cells for an extended time.

Recently, we have used these new tools to study the function of aztreonam (AZT) at the nanometer scale and single living bacteria (*P. aeruginosa*) resolution. AZT is a monocyclic β-lactam antibiotic. It is well-known that the mode of action of AZT is the disruption of the cell wall (*25*). In the previous study, AZT was used to validate Ag nanoparticles as nanometer assays for real-time sizing of membrane porosity and permeability as AZT disrupted the cell walls (*22*). The complete disruption of the cell wall by a high concentration of AZT (31.3 μg/mL) causes the overflowing of intracellular nanoparticles, leading to the aggregation of intracellular Ag nanoparticles.

In this new study, we use this validated nanoparticle assay to study the membrane transport mechanisms of living microbial cells (*P. aeruginosa*) in the absence of antibiotics. In addition, we select an antibiotic (chloramphenicol), which is neither a β-lactam nor aminoglycoside antibiotic. Its primary target in microbial cells is to inhibit the ribosomal peptidyl transferase rather than disrupt the cell wall (*25*). We investigate the dependence of membrane transport upon the dosages of chloramphenicol using single nanoparticle optics and single-living-cell imaging. Furthermore, we select an efflux pump (MexAB−OprM) as a working model and study the role of the efflux pump in controlling the accumulation of substrates (nanoparticles, EtBr, chloramphenicol) in *P. aeruginosa*. In this study, we demonstrate the possibility of real-time sizing of nanoparticles at the nanometer scale using single nanoparticle optics, as these nanoparticles transport through the living microbial cells. We use TEM to determine the size and location of the intracellular Ag nanoparticles at sub-nanometer resolution. We also demonstrate that single Ag nanoparticle optics and single

living cell imaging can be used to monitor the modes of action of antibiotics in real time and probe the new function of antibiotics at single-living-cell resolution with temporal (ms) and size (nm) information. These new tools offer an important new opportunity to advance our understanding of membrane transport kinetics and MDR mechanism in living cells in real time.

MATERIALS AND METHODS

Preparation and Characterization of Nanoparticles. Silver nanoparticles are prepared by reducing $AgNO_3$ aqueous solution with freshly prepared sodium citrate aqueous solution as described in the following (*22*, *24*, *26*). All glassware is well cleaned with aqua regia, rinsed with ultrapure water (Nanopore, 18 MΩ), and then dried prior to the use. We reflux a freshly prepared 500 mL of 1 mM $AgNO_3$ solution in a three-necked round-bottom flask. As the solution is boiling, we add 10 mL of a freshly prepared 1% (w/v) sodium citrate aqueous solution to reduce $AgNO_3$ and generate Ag nanoparticles, leading to a color change of the solution from colorless to greenish-yellow. The solution is refluxed for another hour, cooled to room temperature, and then filtered using a 0.22-μm filter. The Ag nanoparticles are then characterized by optical dark-field microscopy and spectroscopy and transmission electron microscopy (TEM, JEOL 100CX) (*22*, *24*), showing the sizes of the nanoparticles ranging from 20 to 100 nm with an average size of 48 ± 15 nm (Figure 1). Samples for TEM imaging are prepared on 100-mesh Formvar-coated copper grids (Electron Microscopy Sciences).

Ag nanoparticle concentration is determined as 4×10^{-10} M by dividing the moles of nanoparticles by the volume of the solution. The moles of nanoparticles are calculated as follows. The volume of generated Ag is calculated by dividing the weight of Ag generated from the complete reduction of $AgNO_3$ by the density of silver (10.49 g/cm^3). The number of average-size Ag nanoparticles (48 nm) in the solution is computed by dividing the volume of generated Ag with the volume of individual Ag nanoparticles. The moles of Ag nanoparticles are then determined by dividing the number of Ag nanoparticles with Avogadro's constant (6.02×10^{23}).

Chemicals and Supplies. Stock solutions of 2.5 and 25 mg/mL chloramphenicol are prepared by dissolving chloramphenicol in 95% ethanol and by diluting the solution with sterilized ultrapure water as described previously (*27*, *28*). Ethidium bromide (EtBr) solution is prepared in ultrapure water and filtered in triplicate using 0.2-μm sterilized membrane filters (Costar). Quartz slides ($25 \times 75 \times 1$ mm), cover slips ($22 \times 30 \times 0.08$ mm), and nuclepore membranes (25 mm in diameter with 6-μm thickness) are purchased from VWR. A 50 mM phosphate buffer saline (PBS) solution (150 mM NaCl, pH = 7.0) is prepared using ultrapure water. All chemicals, including chloramphenicol, sodium citrate, EtBr, and $AgNO_3$, are purchased from Sigma and used without further purification or treatment.

Cell Culture and Preparation. Cell lines of *P. aeruginosa*, WT (PAO4290, a strain that expresses a wild-type level of MexAB−OprM), nalB-1 (TNP030#1, a mutant that overexpresses MexAB−OprM), and ΔABM (TNP076, a MexAB−OprM deficient mutant), are used (*16*, *29*). Cells are precultured in an Erlenmeyer flask containing 20 mL of L-broth medium (1% tryptone peptone, 0.5% yeast extract, and 0.5% NaCl, pH = 7.2). The flask is then placed in a shaker (Lab-line Orbit Environ-Shaker) (150 rpm, 37 °C) overnight to ensure full growth of the cells. A precultured cell suspension (3 mL) is then transferred to another Erlenmeyer flask containing 20 mL of L-broth medium, which is placed in the shaker (150 rpm, 37 °C) for an additional 8 h to prepare cultured cells. The cultured cells are harvested by centrifugation at 7500 rpm (Beckman Model J2-21 Centrifuge, JA-14 rotor, at 23 °C) for 10 min, washed with 50 mM PBS (pH 7.0) in triplicate, and then resuspended again in the same buffer with cell concentration at $OD_{600\ nm}$ (optical density of cell solution at 600 nm) = 0.1. These cell suspensions are employed for the study of membrane transport using single nanoparticle optics, single living cell imaging and fluorescence spectroscopy, and for the preparation of samples for TEM imaging.

Susceptibility Study. For minimum inhibitory concentration (MIC) measurements, cells are first precultured in L-broth as described above, and then cultured for an additional 8 h in the same medium containing chloramphenicol (0−250 μg/mL) in the presence and absence of 10 μM EtBr or 1.3 pM Ag nanoparticles. The cell growth curves are determined by measuring $OD_{600\ nm}$ of 10× dilutions of the cell culture solutions using a UV−visible spectrometer (Gary 2G, Varian). The plots of $OD_{600\ nm}$ versus chloramphenicol concentration are used to determine the MIC of chloramphenicol for the cells. In addition, a 20-μL aliquot of each cell suspension is imaged in a microchannel using single living cell imaging to study the dependence of cell proliferation upon chloramphenicol concentration. The sealed microchannel is constructed by sandwiching the cell suspension between a microscope slide and a cover slip as described in detail in our previous publications (*18*, *23*, *28*). Using the same approach, the MICs of Ag nanoparticles and EtBr in the absence of chloramphenicol are also measured.

Single Living Cell and Single Nanoparticles Imaging System. Our dark-field optical microscope is equipped with an oil dark-field condenser (Oil 1.43−1.20, Nikon), a 100× objective (Nikon Plan fluor 100x oil, iris, SL. N. A. 0.5−1.3, W. D. 0.20 mm), the microscope illuminator (100 W halogen), a CCD camera (Micromax, 5 MHz Interline, PID 1030 × 1300, Roper Scientific) for high-speed and high-resolution cell imaging, and a color digital camera (Coolpix 990, Nikon) for real-color imaging. Both cameras are added to the microscope through a quad-adapter (Nikon) for real-time imaging. A LN back-illuminated CCD camera (Roper Scientific) coupled with a SpectraPro-150 (Roper Scientific) is added to the microscope using another quad-adapter (Nikon) for simultaneous spectroscopic measurement (*22*, *24*, *30*, *31*). This microscopy and spectroscopy system is capable of real-time imaging of single living cells (*18*, *19*, *28*), imaging and spectroscopic characterization of single nanoparticles (*22*, *24*), and single molecule detection (*23*, *28*, *32*).

Preparation and Imaging of Cell Suspensions. Three milliliters (3 mL) of cell suspension containing 1.3 pM Ag nanoparticles and chloramphenicol (0, 25, and 250 μg/mL) are prepared by mixing 2703 μL of the cell solution ($OD_{600\ nm}$ = 0.1) and 9.8 μL of 0.4 nM Ag nanoparticles, with ultrapure water, 30 μL of 2.5 mg/mL chloramphenicol,

and 30 μL of 25 mg/mL chloramphenicol, respectively. Each suspension is incubated in a vial at 37 °C for 2 h. A 20-μL aliquot of the mixed suspension is sampled at 15 min intervals and directly imaged with 100-ms exposure time in the freshly prepared microchannel using the dark-field microscopy and spectroscopy imaging system equipped with a CCD camera (*18*, *22*). As described previously, the sealed microchannel is constructed by sandwiching the solution between a microscope slide and a cover slip with a 6-μm thick membrane as a spacer (*18*, *23*).

Data Analysis and Statistics of Single Living Cell Imaging. Each full-frame CCD image is able to simultaneously monitor ~60 cells from the cell suspension with $OD_{600\,nm} = 0.1$ (Figure 2). Ten representative images of each suspension at 15-min intervals are recorded over 2 h. Thus, 70 images (~4200 cells) are acquired in total for each solution in 2 h. Each experiment is repeated at least three times; thus, ~12600 cells of each strain of *P. aeruginosa* are studied and analyzed at the single-cell resolution. Images of five representative cells from each suspension are selected to show the intracellular nanoparticles in detail (Figure 3A). Cumulative histograms of the distribution of the number of nanoparticles in the cells versus the nanoparticle sizes are shown in Figure 3B. At every 15 min, 10 images (~600 cells) of each suspension are recorded for each data point in Figure 6. Each experiment is repeated at least three times. Thus, in total ~18000 cells of each strain of *P. aeruginosa* at each 15 min are studied and analyzed at the single-cell resolution.

Ultrathin Sections of Cells for Transmission Electron Microscopy Imaging. A 120-mL aliquot of cell suspension ($OD_{600\,nm} = 0.1$) containing 1.3 pM Ag nanoparticles and chloramphenicol (0, 25, 250 μg/mL) is prepared as described above and incubated in the shaker (150 rpm and 37 °C) for 2 h. Cells are then harvested using centrifugation at 25000 rpm (a Beckman ultra-centrifuge, Ti-50 rotor, at 23 °C) for 30 min. Each pellet is suspended in 1 mL of PBS buffer (pH = 7.0). Each solution is transferred to a sterile microcentrifuge tube. The pellet is collected using centrifugation at 2000 rpm for 5 min and then fixed using 2% gluteraldehyde in PBS buffer at 4 °C overnight. The primary fixative is removed, and the pellet is rinsed with PBS buffer in triplicate with each washing cycle lasting for 10 min. Each pellet is then removed from the microcentrifuge tube and deposited onto a clean microscope slide. A 30-μL aliquot of agar is mixed with each pellet and allowed to solidify. Excess agar is trimmed away from the pellet using a razor blade. Each pellet is then divided into duplicate samples. Each solidified pellet is transferred to a sterile tube. For the secondary fixation at 4 °C for 2 h, 5 mL of 2% OsO_4 in distilled water is added into each tube. The pellets are rinsed using distilled water in triplicate with each washing cycle lasting for 10 min. Pellets are then dehydrated using 25%, 50%, 75%, and 100% ethanol in distilled water (5 mL) for 15 min each (*33*). The pellets are infiltrated using a mixture of resin and acetone (50/50) (EM Bed 812, Ted Pella) at room temperature overnight. The pellets are then infiltrated using 100% resin for 1 h. The pellets are then transferred to embedded molds and embedded in 100% resin. The molds are then placed in an oven to cure at 65 °C for 48 h. Sections with 0.5-μm thicknesses are sliced using an ultramicrotome (RMC MT2C) and examined using an optical microscope to ensure the sample is well prepared. The microsections are then sliced using a diamond knife to prepare 70−80 nm ultrathin layer cross-sections. The nanometer ultrathin sections are mounted on 100-mesh Formvar-coated copper grids, slightly stained with uranyl acetate and lead citrate, and then imaged using the TEM (100CXII, JEOL) with an operating voltage at 60 kV.

Fluorescence Spectroscopic Measurements. Transients of time-dependent fluorescence intensity of EtBr at 590 nm in the absence and presence of chloramphenicol are measured using a fluorescence spectrometer (Perkin-Elmer LS50B) with a time-drive mode at a 3-s data acquisition interval and a 488-nm excitation line. These time-dependent fluorescence intensity transients are used for real-time monitoring of EtBr accumulation kinetics in bulk living cells. The results are used to compare with those measured using single nanoparticle assay and single-living-cell imaging.

RESULTS

Real-Time Sizing Membrane Permeability Using Single Nanoparticle Optics. Silver nanoparticles with diameters 20−100 nm are synthesized as described above (*22*, *26*). These Ag nanoparticles are characterized using dark-field optical microscopy and spectroscopy (localized surface plasmon resonance spectroscopy, LSPRS) and TEM (*22*, *24*) (Figure 1). The full-frame optical image of nanoparticle solution in Figure 1A shows that the solution contains multiple colors of single nanoparticles. The TEM image in Figure 1B indicates that Ag nanoparticles with a variety of sizes are present in the solution, showing that the majority of nanoparticles are spherical while a very few nanoparticles are triangular and hexagonal. The color distribution of single nanoparticles in 0.4 nM solution measured using dark-field microscopy and spectroscopy is used to compare with the size distribution of single nanoparticles from the same solution determined by TEM. The results indicate that the color index of violet, blue, green, and red is correlated with size index of 30 ± 10, 50 ± 10, 70 ± 10, and 90 ± 10 nm, respectively, as we reported previously (*22*). The solution contains approximately 23% of violet (30 ± 10 nm), 53% of blue (50 ± 10 nm), 16% of green (70 ± 10 nm), and 8% of red (90 ± 10 nm) nanoparticles (Supporting Information, Figure 1S).

These multicolored nanoparticles are then used as nanometer-sized probes to directly measure the sizes of substrates that can transport through living microbial membrane, aiming to determine the change of membrane permeability and pore sizes in real time. To minimize the possible effects of competitive transports of nanoparticles with the substrates of interest (e.g., chloramphenicol) and prevent the possible aggregation of nanoparticles, a low concentration of nanoparticles (1.3 pM) is used to incubate with the living cells ($OD_{600\,nm} = 0.1$) for real-time monitoring of membrane transport at the nanometer scale.

Many living individual cells and single nanoparticles in the microchannel are monitored simultaneously using a CCD camera through a dark-field microscope, showing that more nanoparticles are observed in the cells as chloramphenicol concentration increases (Figure 2). Representative images of single cells selected from the full images shown in Figure 3A illustrate the cells containing nanoparticles in detail,

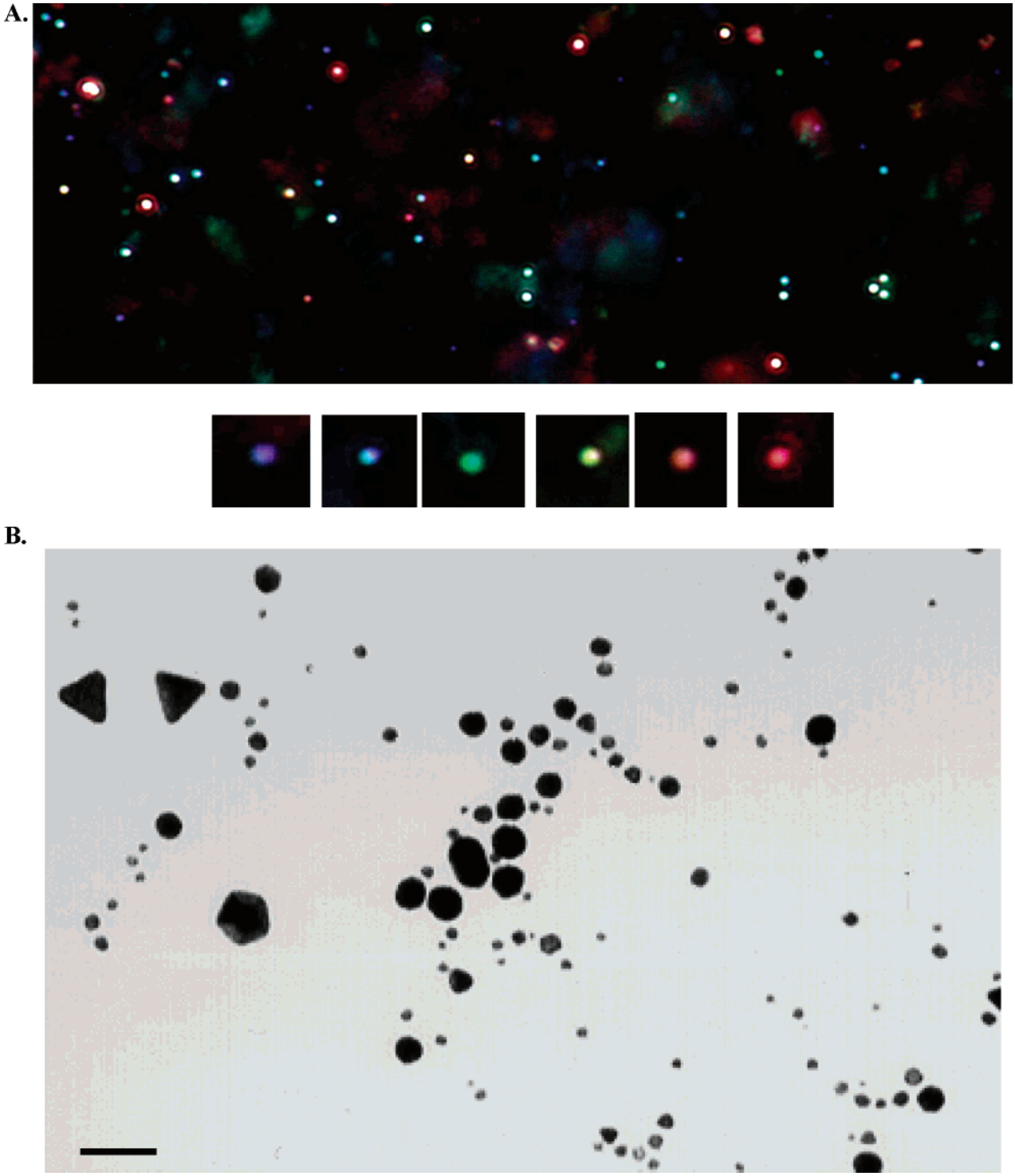

FIGURE 1: Characterization of color index and size index of Ag nanoparticles. (A) The representative full-frame optical image of individual Ag nanoparticles taken from a 0.4 nM Ag nanoparticle solution in a microchannel by a digital color camera through the dark-field optical microscope. Optical images of single Ag nanoparticles selected from the full frame image show the color index of Ag nanoparticles. The optical images of nanoparticles look larger than their actual sizes because of the optical diffraction limit (~200 nm). (B) Representative TEM images of Ag nanoparticles from the solutions in (A) show the sizes and shapes of nanoparticles. The scale bar represents 40 nm.

indicating that more nanoparticles are present in the cells as chloramphenicol concentration increases. Normalized histograms of the number of nanoparticles with the cells versus sizes of the nanoparticles (Figure 3B) indicate that a greater number of larger Ag nanoparticles are with the cells as chloramphenicol concentration increases, suggesting that the permeability and porosity of the cellular membrane increase as chloramphenicol concentration increases. Note that a higher percent of 50 ± 10 nm nanoparticles (53% of the total nanoparticles) are present in the solution. Therefore, more 50 ± 10 nm nanoparticles are observed in the cells. The relative numbers of specific sizes of intracellular nanoparticles in the presence of 0, 25, and 250 μg/mL chloramphenicol are compared to determine the change of membrane permeability and porosity as chloramphenicol concentration increases.

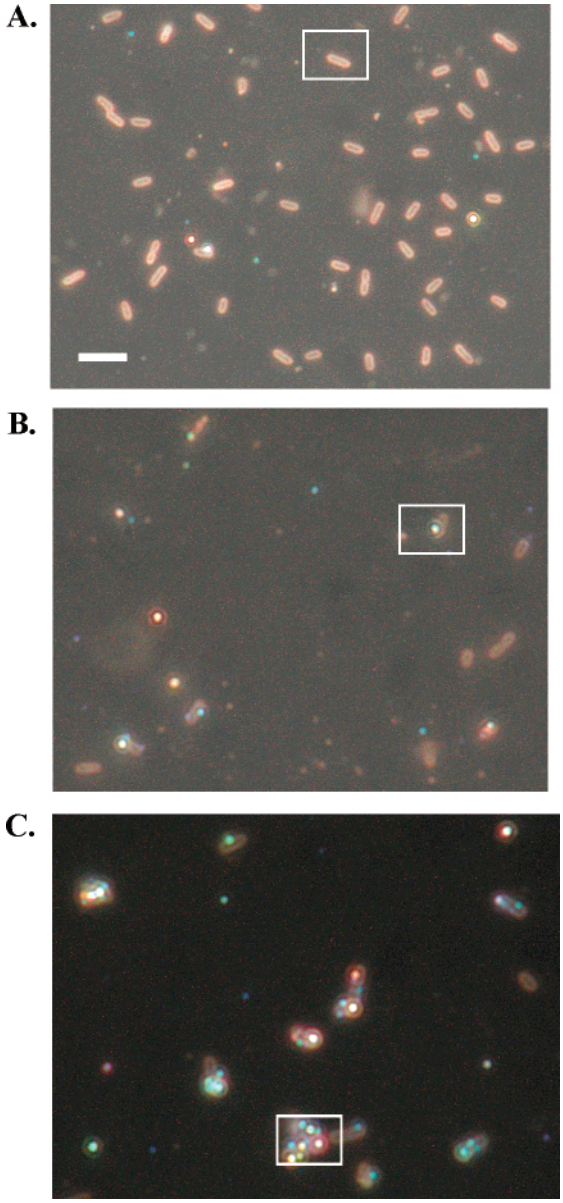

FIGURE 2: Real-time monitoring of membrane transport of many living individual cells (WT) simultaneously in the absence and presence of chloramphenicol using single Ag nanoparticle optics and dark-field optical microscopy. The representative optical images of the cells ($OD_{600\ nm}$ = 0.1) incubated with 1.3 pM Ag nanoparticles and (A) 0, (B) 25, and (C) 250 μg/mL of chloramphenicol in the microchannel, are directly recorded by a color digital camera and CCD camera with 100-ms exposure time. The scale bar represents 4 μm. Each box highlights individual cells: (A) without nanoparticle, (B) with a single Ag nanoparticle, (C) with multiple Ag nanoparticles.

The integrated scattering intensity of selected individual nanoparticles in and out of cells is measured and subtracted from the background in the same image, indicating that the intensity of intracellular nanoparticles is about 10% less than extracellular nanoparticles in the solution and about 20% less than those extracellular nanoparticles on the membrane. The scattering intensity of nanoparticles decreases slightly (~10%) as nanoparticles enter the cellular membrane because the cellular membrane and matrix absorb the microscope illuminator light and reduce its intensity. The decreased intensity of intracellular nanoparticles appears to depend on the location of nanoparticles inside the cells, such as the depth below the cellular membrane. Attempts have been made to quantitatively study the correlation of scattering intensity of intracellular nanoparticles associated with their locations related to the depth below the cellular membrane. Unfortunately, the task becomes impossible because the optical diffraction limit defines the spatial resolution (~200 nm) and makes the nanoparticles appear larger than their actual sizes. Nevertheless, we can qualitatively determine whether the nanoparticles are in or out of the cells based upon their intensity changes as these nanoparticles enter the cells and their transport processes are recorded in real time (*24*).

In addition, the quantum yield of Rayleigh scattering of intracellular Ag nanoparticles is smaller than extracellular Ag nanoparticles because intracellular Ag nanoparticles are surrounded by biomolecules (e.g., proteins, lipids) that reduce the reflection coefficient of Ag nanoparticles (*34*−*37*). Therefore, the nanoparticles outside the cellular membrane appear to radiate more sharply and brightly, whereas nanoparticles inside the cells look blurry and dim as shown in Figure 4. This feature allows us to determine whether the nanoparticles are inside or outside the cells using optical microscopy. The size of the nanoparticles (<100 nm) and the thickness of cell membrane (36 nm including 8 nm inner or outer membrane and ~20 nm between the inner and outer membranes of gram-negative bacteria) are below the optical diffraction limit (~ 200 nm). The scattering intensity of nanoparticles is much higher than that of the cellular membrane because of the higher intrinsic optical dielectric constant of Ag nanoparticles. Therefore, the nanoparticles are much brighter than the membrane, appearing to be accumulated on the membrane (Figure 4B). However, these nanoparticles are blurry, and dimmer than the extracellular nanoparticles, indicating that these blurry nanoparticles are inside the cells. Taken together, the results indicate that, in the absence of chloramphenicol, the majority of red nanoparticles (>80 nm) appear to stay outside the cells, whereas violet, blue, and green nanoparticles (<80 nm) can enter the cells.

To determine the sizes and locations of intracellular nanoparticles at the sub-nanometer (Å) level, ultrathin sections (70−80 nm) of the fixed cells that have been incubated with 1.3 pM nanoparticles and chloramphenicol (0, 25, and 250 μg/mL) for 2 h are prepared and imaged using TEM as described above. TEM images in Figure 5A unambiguously demonstrate that Ag nanoparticles with a variety of sizes (20−80 nm in diameter) are inside the cells in the absence of chloramphenicol. The majority of the nanoparticles are located in the cytoplasmic space of the cells, whereas a few nanoparticles are just underneath the cellular membrane. The cells with embedded triangular nanoparticles (Figure 5A) are particularly selected for easy identification of Ag nanoparticles (Figure 1B). Since the cells are aligned randomly in the embedded resin pellets and are sliced in a random fashion, the shapes of cells are different as shown in Figure 5. The representative cell shapes (e.g., slicing through the vertical or horizontal center of the cells or off the centers of the cells) are selected and shown in Figure 5 to illustrate the positions of the intracellular nanoparticles. Taken together, the TEM images show that the nanoparticles with sizes ranging up to 80 nm are embedded inside the cells in the absence of chloramphenicol, which agrees well with

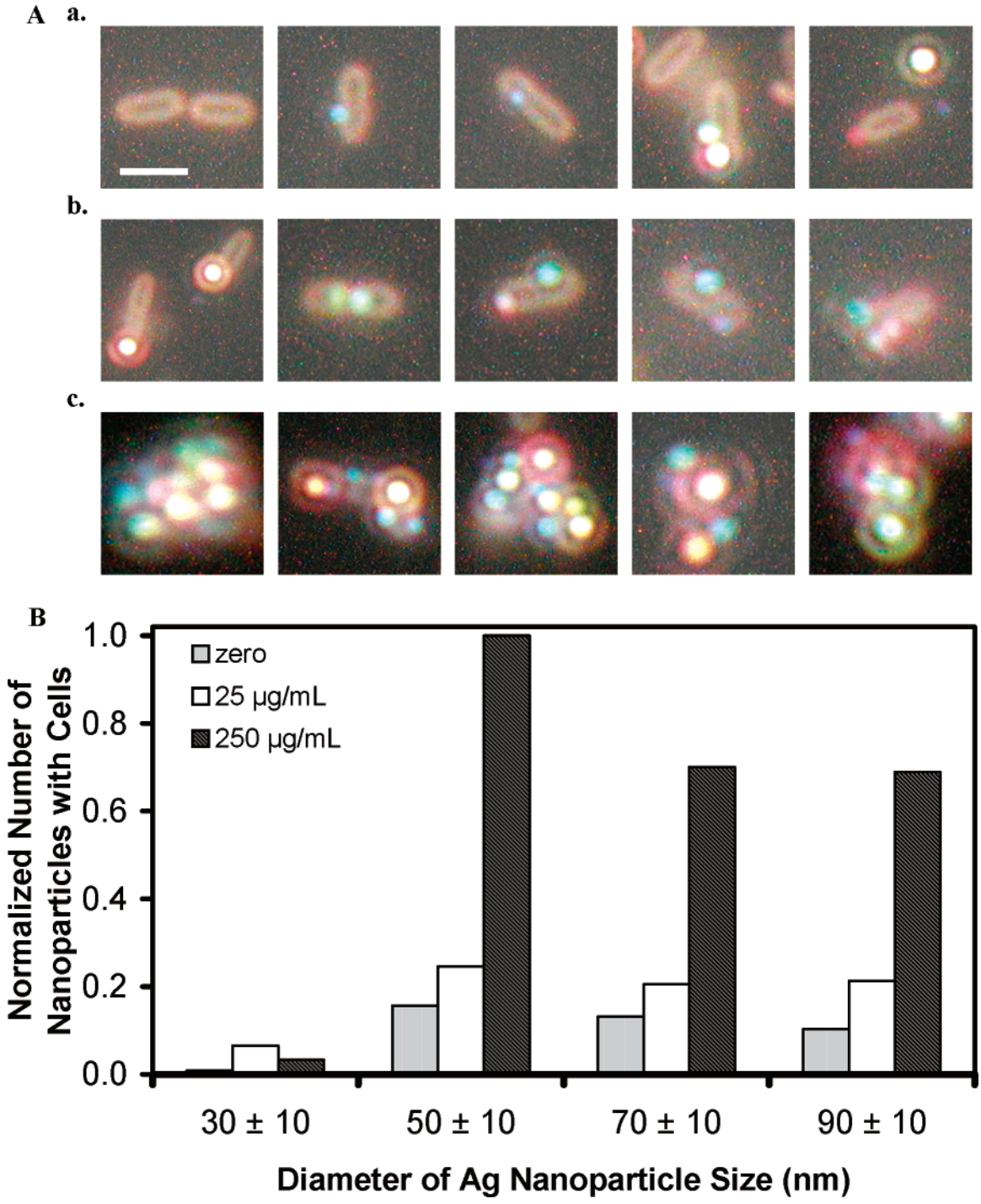

FIGURE 3: Direct observation of real-time change of membrane permeability and pore sizes in WT, induced by chloramphenicol in a dose-dependent manner. (A) Representative optical images (a−c) of single cells selected from ~60 cells in the full-frame images similar to Figure 2. The solutions contain the same concentration of cells ($OD_{600\ nm} = 0.1$) and Ag nanoparticles (1.3 pM), but a different concentration of chloramphenicol: (a) 0, (b) 25, and (c) 250 μg/mL chloramphenicol. Each solution is prepared in a vial and imaged in the microchannel at 15-min intervals for 2 h. The scale bar represents 2 μm. (B) Representative normalized histograms of the number of Ag nanoparticles with the cells versus sizes of nanoparticles from the solutions in (A). Each solution contains the same concentration of cells ($OD_{600\ nm} = 0.1$) and Ag nanoparticles (1.3 pM), but different concentration of chloramphenicol: (a) 0, (b) 25, and (c) 250 μg/mL. The 70 full-frame images (~4200 cells), similar to Figure 2, recorded for 2 h, are analyzed.

those measured using single-nanoparticle optics, suggesting that, even in the absence of chloramphenicol, the nanoparticles with sizes up to 80 nm can transport through the outer and inner cell membrane of *P. aeruginosa*, a size which is about 50 times larger than conventional antibiotics. As chloramphenicol concentration increases to 25 and 250 μg/mL, a greater number of larger Ag nanoparticles are observed inside the cells, suggesting that chloramphenicol increases the membrane permeability and sizes of membrane pores.

To investigate the role of the efflux pump proteins (MexAB−OprM) in controlling the accumulation of intracellular nanoparticles and function of chloramphenicol, we study the membrane permeability of two mutants, nalB-1 (the mutant with the overexpression level of MexAB−OprM)

FIGURE 4: Determination of (A) extracellular and (B) intracellular Ag nanoparticles using the scattering intensity of nanoparticles: optical images of Ag nanoparticles accumulated (A) on membrane (outside the cell) and (B) inside single living cells (*P. aeruginosa*) recorded by digital color camera and CCD camera (exposure time = 100 ms) through the dark-field optical microscope. Extracellular nanoparticles in (A) appear to radiate more sharply and brightly, whereas intracellular nanoparticles in (B) look blurry and dim, indicating that the scattering intensity of nanoparticles decreases as nanoparticles enter the cells, owing to light absorption of cellular membrane and decreased reflection coefficient of intracellular Ag nanoparticles. The scale bars represent 2 μm. The solutions are prepared as described in Figure 3.

and ΔABM (the mutant devoid of MexAB−OprM). Plots of the normalized percent of intracellular Ag nanoparticles versus time for WT, nalB-1, and ΔABM in 0, 25, and 250 μg/mL chloramphenicol, are shown in Figure 6A (a, b, c), 6B (a, b, c), and 6C (a, b, c), respectively. Each data point represents 600 cells in 10 full-frame images, which are acquired in real time as living cells are accumulating intracellular Ag nanoparticles. The nanoparticles transporting in and out of the cells are recorded in real time, resulting in the fluctuation of data points in Figure 6. The number of intracellular Ag nanoparticles in nalB-1 (MexAB−OprM overexpression mutant) appears to highly fluctuate (Figure 6B), which may be attributable to a higher efflux rate of nanoparticles by nalB-1 and suggests that nanoparticles are indeed moving in and out of living cells in real time. Note that these cells are incubated in the PBS buffer solution at room temperature and the cell growth rate in such an environment is negligible. Thus, the cell concentration remains unchanged over the 2-h incubation.

To understand the effect of chloramphenicol upon membrane porosity and transport, the accumulation kinetics of single Ag nanoparticles of WT, nalB-1, and ΔABM in the absence and presence of chloramphenicol (0, 25, and 250 μg/mL) are measured and compared. In the absence of chloramphenicol (Figure 6: a), a very small number of intracellular Ag nanoparticles are observed in WT (Figure 6A: a) and ΔABM (Figure 6C: a), whereas few of intracellular Ag nanoparticles are found in nalB-1 (Figure 6B: a). The number of intracellular Ag nanoparticles in all three strains remains almost unchanged over time. As chloramphenicol concentration increases to 25 μg/mL (Figure 6: b), the number of intracellular Ag nanoparticles in WT (Figure 6A: b) and ΔABM (Figure 6C: b) increases with time at a rate of 4×10^{-5} and 8×10^{-5} s^{-1}, which are about 10-fold higher than in the absence of chloramphenicol, respectively. In contrast, the number of intracellular Ag nanoparticles in nalB-1 (Figure 6B: b) remains almost unchanged over time as observed in the absence of chloramphenicol (Figure 6B: a). As chloramphenicol concentration increases further to 250 μg/mL (Figure 6: c), the number of intracellular Ag nanoparticles in WT (Figure 6A: c) and ΔABM (Figure 6C: c) increases with time at a rate of 1×10^{-4} and 2×10^{-4} s^{-1}, which are about 2.5-fold higher than in 25 μg/mL chloramphenicol, respectively. Unlike those observed in 0 to 25 μg/mL chloramphenicol, the intracellular Ag nanoparticles in nalB-1 (Figure 6B: c) increase with time at the rate of 5×10^{-5} s^{-1}; that is about 2- and 4-fold lower than in WT and ΔABM, respectively.

Taken together, the results show that the number of Ag nanoparticles accumulated in all three strains increases as chloramphenicol concentration increases and as incubation time increases, suggesting that chloramphenicol increases membrane porosity and permeability (Figure 6). In addition, the results indicate that accumulation kinetics of intracellular nanoparticles is associated with the expression levels of MexAB−OprM. The mutant with the overexpression level of MexAB−OprM (nalB-1) accumulates the least number of intracellular Ag nanoparticles, whereas the mutant devoid of MexAB−OprM (ΔABM) accumulates the greatest number of Ag nanoparticles. This suggests that MexAB−OprM plays a critical role in controlling of accumulation of intracellular Ag nanoparticles.

Fluorescence Spectroscopic Measurements. To rule out the possibility of steric and size effect of using Ag nanoparticle probes for real-time sizing of membrane permeability and porosity induced by chloramphenicol (antibiotic), we use a small molecule (EtBr) as a fluorescence probe and measure accumulation kinetics of EtBr by bulk WT, nalB-1, and ΔABM in the presence of 0, 25, and 250 μg/mL chloramphenicol. EtBr and chloramphenicol enter the cells through passive diffusion and are extruded out of the cells by the efflux pumps in *P. aeruginosa* (*29*, *38*, *39*, *40*). The EtBr concentration at 10 μM is deliberately selected to be much lower than chloramphenicol concentration, 25 μg/mL (77 μM) and 250 μg/mL (770 μM), allowing chloramphenicol to dominate the passive diffusion pathway and enter the cells. This approach minimizes the possible effect of the presence of EtBr on the accumulation of chloramphenicol, ensuring the function of chloramphenicol to be studied using EtBr.

Transients of time-dependent fluorescence intensity of EtBr at 590 nm from the solutions containing 10 μM EtBr and the cells (WT, nalB, and ΔABM) in the absence and presence of chloramphenicol (0, 25, and 250 μg/mL) are shown in Figure 7, panels A, B, and C, respectively. The

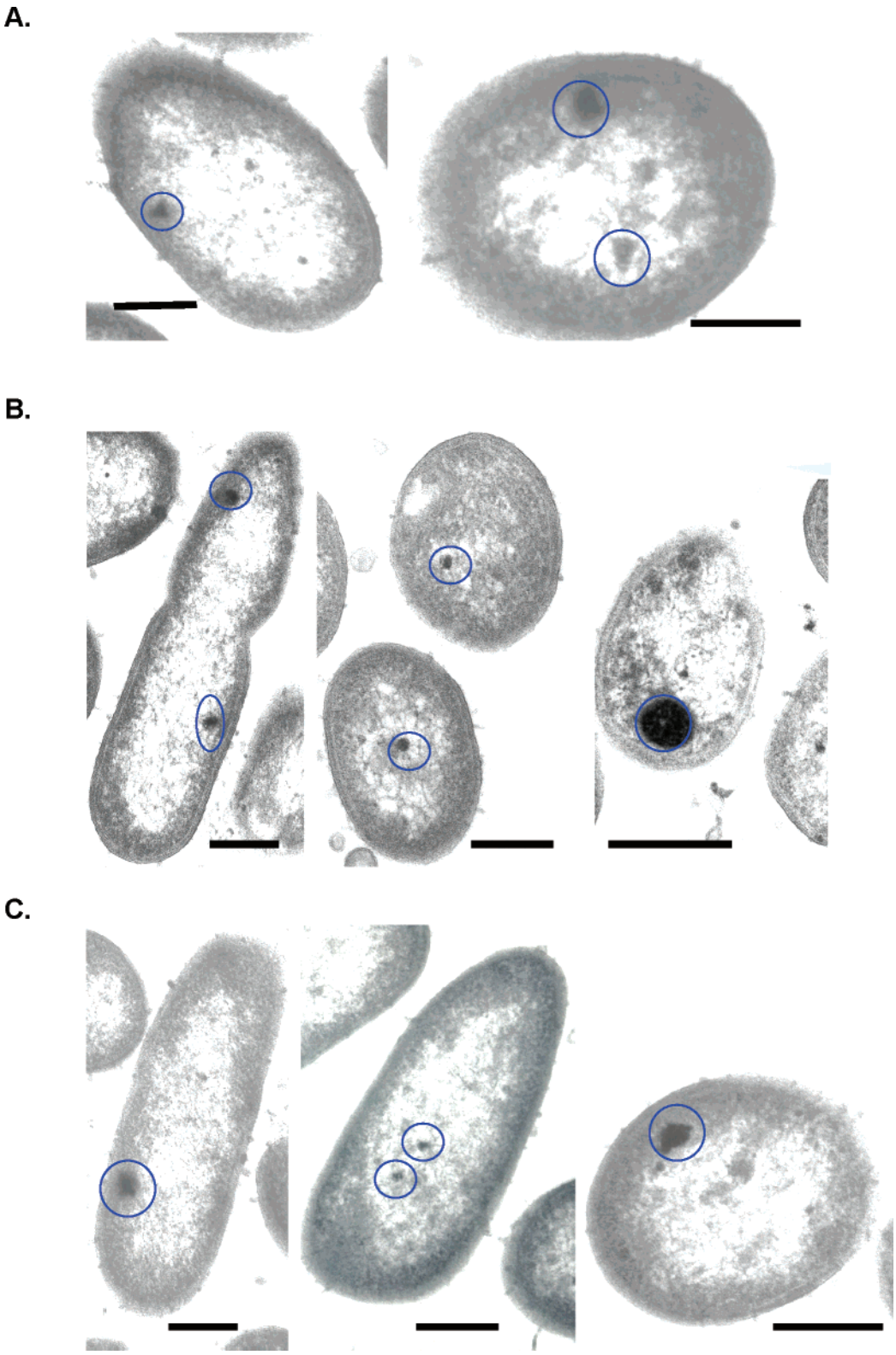

FIGURE 5: TEM images show sizes and locations of Ag nanoparticles inside the cells (WT), which are acquired from ultrathin cross-sections (70−80 nm) of fixed WT cells sliced by a diamond knife. The cells ($OD_{600\ nm}$ = 0.1) have been incubated with 1.3 pM Ag nanoparticles and (A) 0, (B) 25, and (C) 250 μg/mL chloramphenicol for 2 h before fixation, as described in the text. The scale bars represent 220 nm, and the circles are used to highlight the nanoparticles.

changes of fluorescence intensity over time are used to real-time monitor the accumulation kinetics of EtBr in the cells because EtBr enters the cells and intercalates with DNA, leading to a 10-fold increase in fluorescence intensity. The accumulation rate of EtBr in 0, 25, and 250 μg/mL chloramphenicol are measured and compared to determine the dose effect of chloramphenicol upon the membrane permeability. The initial fluorescence intensity of each cell type is varied slightly, which may be attributable to the variation of cell concentration ($OD_{600\ nm}$ = 0.1 ± 0.02), distribution of cell sizes (1−2 μm), and the fluctuation of excitation intensity of the Xe lamp in fluorescence spec-

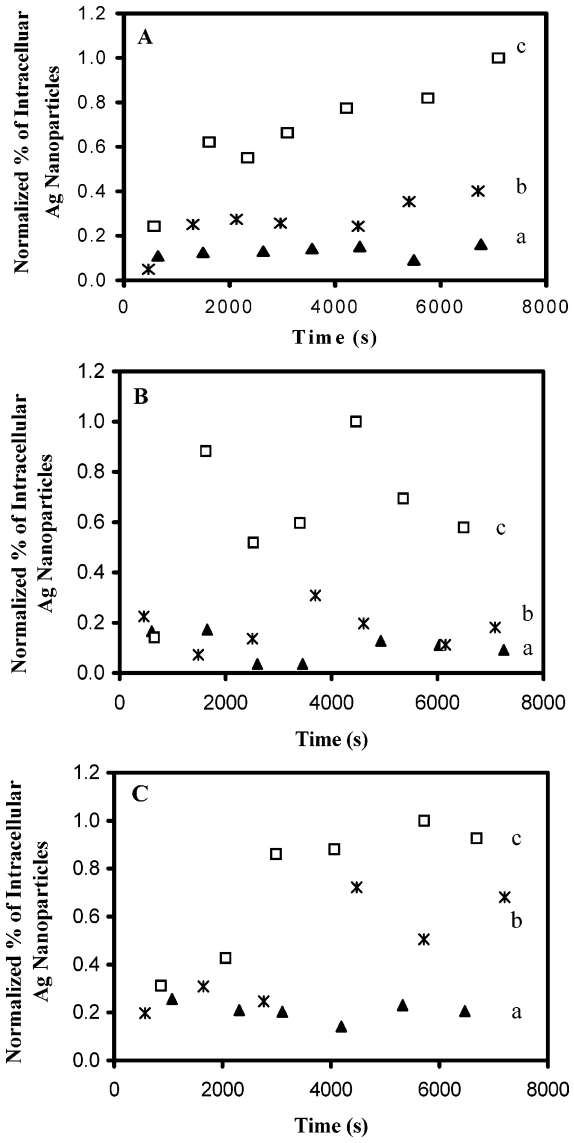

FIGURE 6: Real-time measurements of accumulation kinetics of single Ag nanoparticles in living cells, showing that membrane permeability and porosity increase as chloramphenicol concentration increases. Plots of normalized number of intracellular Ag nanoparticles versus time: (A) WT, (B) nalB-1, and (C) ΔABM, from solution containing the cells ($OD_{600\,nm}$ = 0.1); 1.3 pM Ag nanoparticles, and (a, ▲) 0, (b, *) 25, and (c, □) 250 μg/mL chloramphenicol. Ten full-frame images of each solution are acquired at 15-min intervals and each image is recorded with 100-ms exposure time. Each data point represents 600 cells.

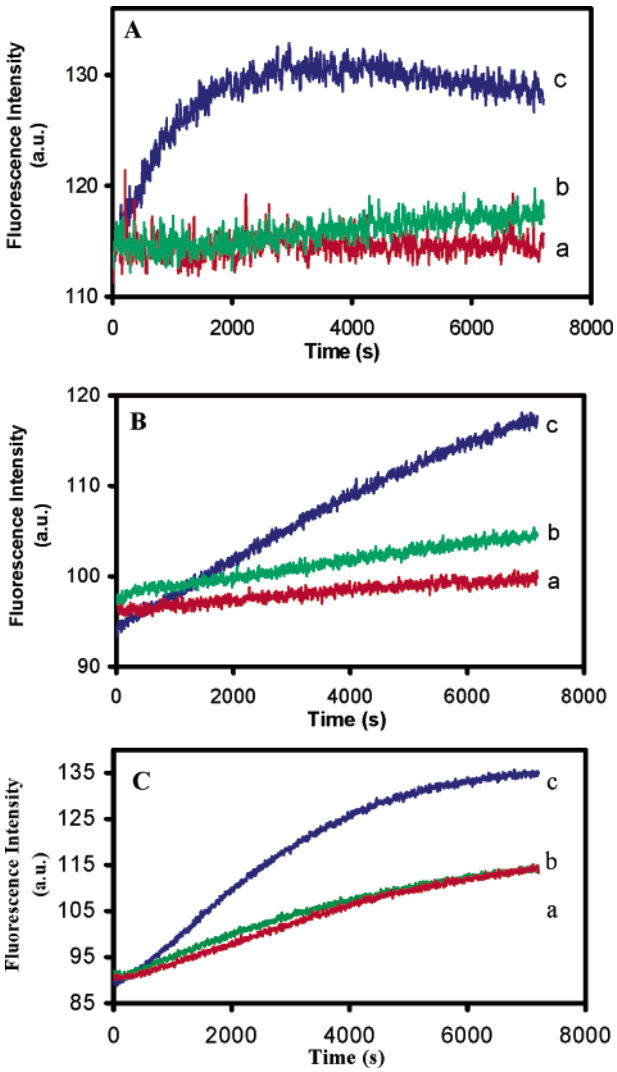

FIGURE 7: Real-time monitoring of EtBr accumulation kinetics in living cells. Representative transients of time-dependent fluorescence intensity of EtBr at 590 nm from the 3.0-mL solutions containing 10 μM EtBr and the cells ($OD_{600\,nm}$ = 0.1): (A) WT, (B) nalB-1, and (C) ΔABM; and (a) 0, (b) 25, and (c) 250 μg/mL chloramphenicol, respectively. Each transient is acquired from the 3.0-mL solution in a quartz cuvette using fluorescence spectroscopy with time-drive mode at a 3-s data acquisition interval and 488-nm excitation.

trometer. It is also important to point out that these cells only grow and divide in cell culture medium. In these experiments, the cells are incubated in the PBS buffer solution at room temperature and the cells do not grow and divide significantly in such an environment. Thus, the cell concentration remains unchanged over the 2-h incubation.

In the absence of chloramphenicol (Figure 7: a), the transients of time-dependent fluorescence intensity of EtBr in nalB-1, WT, and ΔABM, show that fluorescence intensity increases with time at a rate of 5×10^{-4}, 5×10^{-4}, and 4×10^{-3} s^{-1}, respectively, suggesting that ΔABM accumulates EtBr approximately 10 times (Figure 7C: a) faster than WT (Figure 7A: a) and nalB-1 (Figure 7B: a). As chloramphenicol concentration increases to 25 μg/mL (Figure 7: b), the fluorescence intensity increases with time at a rate of 9×10^{-4}, 6×10^{-4}, and 5×10^{-3} s^{-1}, which is slightly (1.8, 1.2, and 1.3 times) higher than those observed in the absence of chloramphenicol, for bulk WT, nalB-1, and ΔABM, respectively. In contrast, as chloramphenicol concentration increases further to 250 μg/mL (Figure 7: c), fluorescence intensity increases with time at a rate of 3×10^{-3}, 9×10^{-3}, and 1×10^{-2} s^{-1}, showing 3, 18, and 2 times faster than in 25 μg/mL chloramphenicol, for nalB-1, WT, and ΔABM, respectively. The rates of increased fluorescence intensity of EtBr in ΔABM (Figure 7C: c) are 1.1 times and 3.3 times faster than in WT (Figure 7A: c) and nalB-1 (Figure 7B: c), respectively.

Taken together, the result shows that the mutant devoid of MexAB−OprM (ΔABM) accumulates EtBr most rapidly, whereas the mutant with the overexpression level of MexAB−OprM (nalB-1) accumulates EtBr most slowly. This suggests that MexAB−OprM plays an important role in controlling the accumulation of EtBr, as reported previously (*13*, *17*,

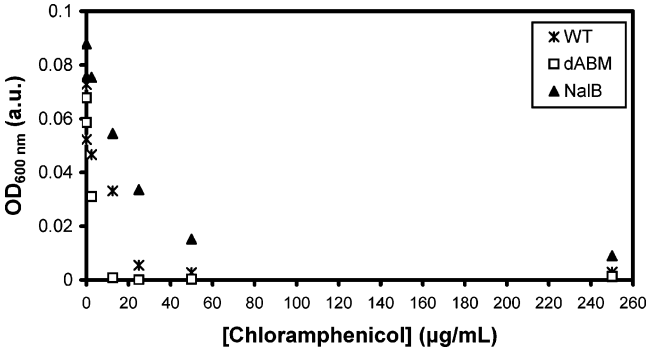

FIGURE 8: Determination of minimum inhibitory concentration (MIC) of chloramphenicol for WT, nalB-1, and ΔABM. Representative plots of $OD_{600\ nm}$ versus chloramphenicol concentration (0, 2.5, 12.5, 25, 50, and 250 μg/mL) from the solutions containing 10 μM EtBr and ΔABM (□), WT (*), and nalB-1 (▲), indicating that the MIC of ΔABM, WT, and nalB-1 is 12.5, 25, and 250 μg/mL, respectively. The MICs are also confirmed at single cell resolution using single living cell imaging (Figure 2S).

18, *23*). These results agree qualitatively with those measured using single-nanoparticle optics and single-living-cell imaging (Figure 6), validating that single Ag nanoparticles can be used as nanometer probes for real-time sizing membrane transport in living cells. Unlike the accumulation kinetics measured using fluorescence probes (EtBr), the results acquired by single nanoparticles and single living cell images offer new insights into the change of membrane permeability and pore sizes at the nanometer scale (Figures 3 and 4). For example, Ag nanoparticles with a size beyond 80 nm (red nanoparticle) appear to be difficult to transport through the membrane of *P. aeruginosa* in the absence of chloramphenicol (Figure 4). In contrast, a greater number of larger nanoparticles are accumulated in living cells as chloramphenicol concentration increases (Figure 3), suggesting that chloramphenicol increases the membrane permeability and pore sizes.

Susceptibility Measurements. If Ag nanoparticles or EtBr compete with chloramphenicol for membrane transport and accumulation in the cells, such competition would have led to decreased accumulation of chloramphenicol in the cells and hence changed the susceptibility of chloramphenicol. To rule out the possibility of such competitive accumulation in the cells, the MIC of chloramphenicol in the presence of 10 μM EtBr is determined by measuring the optical density (OD) of the cell suspension at 600 nm and imaging individual living cells in the cell suspension. Note that $OD_{600\ nm}$ and single-living-cell imaging are applied to determine the number of cells that have survived in the presence of particular concentration of chloramphenicol. Plots of $OD_{600\ nm}$ of bulk cell suspension versus chloramphenicol concentration (0, 2.5, 12.5, 25, 50, 250 μg/mL) in Figure 8 indicate that MIC of 12.5, 25, and 250 μg/mL chloramphenicol for ΔABM, WT, and nalB-1 cells, respectively. Single-living-cell imaging is used to directly observe the number of survival cells in the presence of chloramphenicol (0, 2.5, 12.5, 25, 50, 250 μg/mL) at single-cell resolution. Ten images are taken for each chloramphenicol concentration and each experiment is repeated in triplicate. Thus, 30 images of each chloramphenicol concentration are acquired to determine the number of survival cells, showing few cells have survived in the presence of the minimum concentration of chloramphenicol at 12.5, 25, and 250 μg/mL for ΔABM, WT, and nalB-1, respectively (Supporting Information, Figure 2S). The result further confirms the MIC measured using $OD_{600\ nm}$ (Figure 8). Similar results are observed in the experiments involving 1.3 pM Ag nanoparticles (*41*). These MIC results agree well with the MICs measured in the absence of EtBr and Ag nanoparticles (*28*, *38*), indicating that the presence of 10 μM EtBr or 1.3 pM Ag nanoparticles does not significantly affect the accumulation of chloramphenicol in the cells and neither 10 μM EtBr nor 1.3 pM Ag nanoparticles cause significant toxicity to the living cells. The results also show that the MICs are highly associated with the expression level of the MexAB−OprM, indicating that the mutant devoid of MexAB−OprM (ΔABM) accumulates chloramphenicol most effectively, leading to the lowest MIC at 12.5 μg/mL. In contrast, the mutant with overexpression of MexAB−OprM (nalB-1) accumulates chloramphenicol least effectively, leading to the highest MIC at 250 μg/mL.

MICs of EtBr and Ag nanoparticles in the absence of chloramphenicol are also measured using the same approach, showing that MICs of EtBr and Ag nanoparticles for all three strains are higher than 10 μM and 1.3 pM, respectively (41). The study of MIC and biocompatibility of Ag nanoparticles in the absence of chloramphenicol is described in detail elsewhere (*41*). Taken together, the results of the MIC experiments further demonstrate that the presence of 1.3 pM Ag nanoparticles or 10 μM EtBr does not appear to interfere the accumulation of chloramphenicol in the cells. Therefore, this experiment further validates that 1.3 pM Ag nanoparticles can be used as nanometer probes to study membrane transport in the living cells.

DISCUSSION

Optical properties (colors, LSPRS) of Ag nanoparticles depend on size and shape of nanoparticles and the dielectric constant of the embedded medium (*34*−*37*, *42*). Unlike the bulk plasmon, the surface plasmon of nanoparticles can be directly excited by propagating light waves (electromagnetic waves), leading to the selective absorption and scattering of light. Therefore, the colors (LSPRS) of Ag nanoparticles are correlated with the sizes of nanoparticles, while the shape of nanoparticles and their embedded medium remain unchanged (Figure 1) (*22*, *24*). Such unique size-dependent optical properties allow us to use the color index of nanoparticles (violet, blue, green, red) as the nanometer size index probes (30 ± 10, 50 ± 10, 70 ± 10, 90 ± 10 nm) for real-time sizing the change of living cellular membrane permeability and porosity at the nanometer scale.

Individual Ag nanoparticles are extremely bright under dark-field optical microscope and can be directly imaged by a digital or CCD camera through the dark-field microscope. Unlike fluorescence dyes, these nanoparticles do not suffer photodecomposition and can be used as a probe to continuously monitor dynamics and kinetics of membrane transport in living cells for an extended time (hours). In addition, these nanoparticles can be used as nanometer probes to determine the sizes of substrates that are transporting in and out of the living cellular membrane at the nanometer scale in real time.

The scattering intensity of the nanoparticles decreases as nanoparticles enter the cell membrane and move into the cytoplasmic space, because the cellular membrane and matrix absorbs the light of the microscope illuminator and reduces

its intensity. Furthermore, the intracellular nanoparticles are surrounded by a cellular matrix (e.g., proteins, lipids) inside the cells, and hence the reflection coefficient of intracellular Ag nanoparticles is smaller than the extracellular Ag nanoparticles (*34*−*36*). With an imaging system that is sufficiently sensitive to detect single fluorescence dye molecules (*19*, *28*, *32*), intracellular and extracellular single Ag nanoparticles with diameters at 20−100 nm are easily observed and distinguished (Figures 3 and 4). Since the size of the nanoparticles and thickness of the cellular membrane are under the optical diffraction limit (∼200 nm), the intracellular nanoparticles appear accumulated on the membrane (Figure 4B). However, these nanoparticles appear blurry and dimmer than the extracellular nanoparticles, indicating that the blurry nanoparticles are inside the cells.

TEM is used to confirm the intracellular nanoparticles inside the cells at subnanometer (Å) resolution. The TEM images of ultrathin cross-sections of cells with nanoparticles in Figure 5 unambiguously illustrate that the nanoparticles with sizes up to 80 nm in diameter are observed inside the cells in the absence of chloramphenicol. The majority of nanoparticles (20−80 nm) are in the cytoplasmic space of the cells, whereas some of nanoparticles are right underneath the cellular membrane. This finding suggests that the outer and inner membrane of *P. aeruginosa* permeate the substrates with sizes up to 80 nm, which are 50 times larger than conventional antibiotics and detergents.

Bulk cells are monitored simultaneously at the single-cell resolution using single-living-cell imaging (Figure 2). Accumulation kinetics of nanoparticles in living cells is measured in real time using single nanoparticle optics. Even though these nanoparticles look larger than their actual sizes due to the optical diffraction limit, the sizes of nanoparticles are determined using their colors (LSPRS). As chloramphenicol concentration increases to 25 and 250 μg/mL, more nanoparticles are observed in the cells, suggesting that the membrane permeability and porosity increase. As more nanoparticles are accumulated in the cells, it becomes more difficult to distinguish individual nanoparticles. Nevertheless, the sizes of individual intracellular nanoparticles can still be distinguished using their colors (LSPRS) even in the presence of 250 μg/mL of chloramphenicol, suggesting that chloramphenicol increases membrane permeability but does not completely disrupt the cell walls. Such observations are distinguished from our previous study of the function of AZT (β-lactam antibiotic) in which AZT completely disrupted the cell walls and individual intracellular Ag nanoparticles were aggregated and hard to distinguish in the presence of 31.3 μg/mL of AZT (*22*).

Chloramphenicol is neither a β-lactam nor an aminoglycoside antibiotic. Its primary target is ribosomal peptidyl transferase, where it acts competitively to inhibit normal substrate binding and protein synthesis (*25*). This study suggests that chloramphenicol also leads to increased membrane permeability. These new insights further demonstrate the unique advantages of using single nanoparticles as probes for the study of function of antibiotics and membrane transport. The plausible explanation for such a mode of action of chloramphenicol is that chloramphenicol inhibits the protein synthesis, leading to disintegration of the membrane and increased membrane permeability (*28*).

The accumulation rate of intracellular nanoparticles shows mutant dependence (Figure 6), indicating that the mutant devoid of MexAB−OprM (ΔABM) accumulates the nanoparticles most rapidly, whereas MexAB−OprM overexpression mutant (nalB-1) accumulates the nanoparticles most slowly. This result suggests that MexAB−OprM plays an important role in controlling the accumulation of nanoparticles in the cells. Nanoparticles are much larger substrates than conventional drugs (e.g., antibiotics, dyes). It is surprising that the nanoparticles (up to 80 nm) permeate through the cellular membrane. These are bacterial cells. Currently, there is no evidence available to support the process of endocytosis, pinocytosis, or exocytosis in prokaryotes (*P. aeruginosa*). However, it is well-known that MexAB−OprM can extrude a wide spectrum of substrates, such as antibiotics, dyes, detergents, and chemotoxic materials, out of the cells using the proton motive force as the energy source (*7*, *8*). Therefore, one plausible suggestion for the transport mechanism of nanoparticles through the living cellular membrane is that nanoparticles enter the cells through passive diffusion and are most likely extruded out of the cells by the extrusion mechanism of bacteria. Even though the sizes of Ag nanoparticles seem 50 times larger than the pore sizes of membrane pumps (MexAB−OprM), it is possible that the substrates (nanoparticles) can induce the assembly of the pumps in real time and define the pore sizes of the pumps. Currently, the crystal structure of the membrane pump is unavailable and the extrusion mechanism of the pump still remains essentially unknown (*1*, *6*). On the other hand, it is also possible that Ag nanoparticles may enter the cells and are extruded out of the cells using unidentified pathways. Our works are in progress to further understand potential pathways that lead to the entry and efflux of megasubstrates (nanoparticles) of bacteria.

EtBr has been widely used as a fluorescence probe for the study of membrane permeability and extrusion machinery of bacterial cells (*15*, *17*, *18*, *23*). EtBr is an especially suitable fluorescence probe for such study because EtBr emits weaker fluorescence in an aqueous environment (outside the cells) and becomes ten times more strongly fluorescent as it enters the cells and intercalates with DNA in the cells (*43*). It is well-known that EtBr enters the cells using passive diffusion and is extruded out of cells by efflux pumps of *P. aeruginosa* using a proton motive force as an energy source (*15*−*17*).

The fluorescence spectra of EtBr indicate that the emission peak at 590 nm remains unchanged in a 2 h incubation of EtBr with the living cells (*17*, *23*). Therefore, the transients of time-dependent fluorescence intensity at 590 nm are used to measure the accumulation kinetics of living cells, showing that fluorescence intensity increases with time more rapidly as chloramphenicol concentration increases and demonstrating that chloramphenicol increases membrane permeability (Figure 7). The time-dependent fluorescence intensity transients also show the mutant dependence, indicating that the mutant devoid of MexAB−OprM (ΔABM) accumulates EtBr most rapidly, whereas the mutant with overexpression of MexAB−OprM (nalB-1) accumulates EtBr most slowly, suggesting that MexAB−OprM plays a leading role in the accumulation of substrate (EtBr) in the cells. Taken together, accumulation kinetics measured using EtBr (a small fluorescence molecule) in Figure 7 is consistent with those

observed using single nanoparticles (Figure 6), eliminating the concern of the possible steric and size effects of using large nanoparticle probes for the study of membrane transport mechanism in living cells.

The MICs of chloramphenicol in the presence of 10 μM EtBr or 1.3 pM Ag nanoparticles also show the mutant dependence, indicating an MIC of 12.5, 25, and 250 μg/mL for ΔABM, WT, and nalB-1, respectively (Figures 8 and 2S). The MICs agree well with those measured in the absence of EtBr and Ag nanoparticles (*23*, *29*, *38*, *41*), further suggesting that the presence of 10 μM EtBr or 1.3 pM Ag nanoparticles neither affect the accumulation of chloramphenicol in the cells nor create significant toxicity to the cells. This result further confirms that a low concentration of Ag nanoparticles (1.3 pM) can be used as a powerful nanoprobes to real-time study membrane transport in living microbial cells.

Unlike fluorescence probes, Ag nanoparticles can offer real-time size information of the substrates that transport through living cell membranes at the nanometer scale. Because the color (LSPRS) index of nanoparticles can be used as the nanometer size index, the accumulation kinetics can be measured at the millisecond temporal resolution using dark-field optical microscopy and spectroscopy. In addition, the scattering intensity of Ag nanoparticles decreases slightly (∼10%) as nanoparticles just pass through the membrane and enter the cells, offering the opportunity to trace the transport of nanoparticles in and out of the membrane. Furthermore, the scattering intensity of Ag nanoparticles does not decay over time, owing to their resistance to photodecomposition. Taken together, these unique characteristics of Ag nanoparticles allow multiple sizes (multiple colors) of Ag nanoparticles to be used as the nanometer probes to determine the sizes of transport substrates and measure membrane permeability and porosity in living cells for an extended time.

CONCLUSION

In summary, we have developed and applied single-Ag-nanoparticle optics and single-living-cell imaging to investigate membrane transport in living microbial cells (*P. aeruginosa*) in real time.

New findings from this study include the following. (i) In the absence of antibiotics, Ag nanoparticles with sizes up to 80 nm can transport through the inner and outer cellular membrane of *P. aeruginosa*, about 50 times larger than conventional antibiotics. The majority of the intracellular Ag nanoparticles are located in the cytoplasmic space of the cells, whereas a few nanoparticles are just underneath the cellular membrane. (ii) The accumulation kinetics of intracellular Ag nanoparticles measured using single nanoparticle optics are similar to the accumulation kinetics of EtBr (a small fluorescence molecule), validating Ag nanoparticles as nanoprobes to measure membrane transport mechanisms of microbial cells in real time. Unlike fluorescence probes, Ag nanoparticle probes can measure the change of membrane permeability and pore sizes at the nanometer scale for an extended time. (iii) Single nanoparticle optics and single-living-cell imaging can be used to investigate the new function of antibiotics. For example, this study indicates that chloramphenicol increases the membrane permeability in a dose-dependent manner, which has not been reported previously. (iv) MICs of chloramphenicol in the absence and presence of 1.3 pM Ag nanoparticles or 10 μM EtBr remain the same, indicating that neither 1.3 pM Ag nanoparticles nor 10 μM EtBr affects the accumulation of chloramphenicol in the cells and suggesting that neither 1.3 pM Ag nanoparticles nor 10 μM EtBr create significant toxicity to the cells. Taken together, this study further demonstrates that a low concentration of Ag nanoparticles (1.3 pM) can be used as powerful nanoprobes to study membrane transport in living microbial cells.

ACKNOWLEDGMENT

We thank Taiji Nakae and Hiroshi Yoneyama (Tokai University School of Medicine, Japan) for three strains of *P. aeruginosa* and helpful discussion and Keith Carson, Denise Sliter, and Rudrax Patel for assistance of TEM experiments.

SUPPORTING INFORMATION AVAILABLE

Characterization of silver (Ag) nanoparticles shown in detail (Figure 1S), demonstrating that the color index of Ag nanoparticles is associated with size index of Ag nanoparticles. Determination of minimum inhibitory concentration (MIC) of chloramphenicol in the presence of 10 M EtBr for WT, nalB-1, and ΔABM using single living cell imaging (Figure 2S). This material is available free of charge via the Internet at http://pubs.acs.org.

REFERENCES

1. Ryan, B. M., Dougherty, T. J., Beaulieu, D., Chuang, J., Dougherty, B. A., and Barrett, J. F. (2001) Efflux in bacteria: what do we really know about it? *Expert Opin. Invest. Drugs 10* (7), 1409−1422, and references therein.
2. Nakae, T. (1997) Multiantibiotic resistance caused by active drug extrusion in *Pseudomonas aeruginosa* and other gram-negative bacteria, *Microbiologia 13* (3), 273−284, and references therein.
3. Poole, K. (2001) Multidrug efflux pumps and antimicrobial resistance in *Pseudomonas aeruginosa* and related organisms, *J. Mol. Microbiol. Biotechnol. 3* (2), 255−264.
4. Cole, S. P., Bhardwaj, G., Gerlach, J. H., Mackie, J. E., Grant, C. E., Almquist, K. C., Stewart, A. J., Kurz, E. U., Duncan, A. M., and Deeley, R. G. (1992) Overexpression of a transporter gene in a mutidrug-resistant human lung cancer cell line, *Science 258*, 1650−1654.
5. Paulsen, I. T., Sliwinski, M. K., and Saier, M. H., Jr. (1998) Microbial genome analyses: comparative transport capabilities in eighteen prokaryotes, *J. Mol. Biol. 277*, 573−592.
6. Stover, C. K., Pham, X. Q., Erwin, A. L., Mizoguchi, S. D., Warrener, P., Hickey, M. J., Brinkman, F. S., Hufnagle, W. O., Kowalik, D. J., Lagrou, M., Garber, R. L., Goltry, L., Tolentino, E., Westbrock-Wadman, S., Yuan, Y., Brody, L. L., Coulter, S. N., Folger, K. R., Kas, A., Larbig, K., Lim, R., Smith, K., Spencer, D., Wong, G. K., Wu, Z., and Paulsen, I. T. (2000) Complete genome sequence of *Pseudomonas aeruginosa* PA01, an opportunistic pathogen, *Nature 406*, 959−964.
7. Ma, D., Cook, D. N., Hearst, J. E., and Nikaido, H. (1994) Efflux pumps and drug resistance in gram-negative bacteria, *Trends Microbiol. 2* (12), 489−493.
8. Maseda, H., Yoneyama, H., and Nakae, T. (2000) Assignment of the substrate-selective subunits of the MexEF−OprN multidrug efflux pump of *Pseudomonas aeruginosa*, *Antimicrob. Agents Chemother*. *44* (3), 658−664.
9. Masuda, N., Sakagawa, E., Ohya, S., Gotoh, N., Tsujimoto, H., and Nishino, T. (2000) Substrate specificities of MexAB−OprM, MexCD-OprJ, and MexXY-oprM efflux pumps in *Pseudomonas aeruginosa*, *Antimicrob. Agents Chemother. 44* (12), 3322−3327.
10. Germ, M., Yoshihara, E., Yoneyama, H., and Nakae, T. (1999) Interplay between the efflux pump and the outer membrane

permeability barrier in fluorescent dye accumulation in *Pseudomonas aeruginosa*, *Biochem. Biophys. Res. Commun. 261* (2), 452−455.
11. Lee, A., Mao, W., Warren, M. S., Mistry, A., Hoshino, K., Okumura, R., Ishida, H., and Lomovskaya, O. (2000) Interplay between efflux pumps may provide either additive or multiplicative effects on drug resistance, *J. Bacteriol. 182* (11), 3142−3150.
12. Lei, Y., Sato, K. and Nakae, T. (1991) Ofloxacin-resistant *Pseudomonas aeruginosa* mutants with elevated drug extrusion across the inner membrane, *Biochem. Biophys. Res. Commun. 178* (3), 1043−1048.
13. Lomovskaya, O., Warren, M. S., Lee, A., Galazzo, J., Fronko, R., Lee, M., Blais, J., Cho, D., Chamberland, S., Renau, T., Leger, R., Hecker, S., Watkins, W., Hoshino, K., Ishida, H. and Lee, V. J. (2001) Identification and characterization of inhibitors of multidrug resistance efflux pumps in *Pseudomonas aeruginosa*: novel agents for combination therapy, *Antimicrob. Agents Chemother. 45* (1), 105−116.
14. Nakae, T. (1995) Role of membrane permeability in determining antibiotic resistance in *Pseudomonas aeruginosa*, *Microbiol. Immunol. 39* (4), 221−229, and references therein.
15. Mortimer, P. G., and Piddock, L. J. (1991) A comparison of methods used for measuring the accumulation of quinolones by Enterobacteriaceae, *Pseudomonas aeruginosa* and *Staphylococcus aureus*, *J. Antimicrob. Chemother. 28* (5), 639−653.
16. Ocaktan, A., Yoneyama, H., and Nakae, T. (1997) Function of the membrane fusion protein, MexA, of the MexA, B.-OprM efflux pump in *Pseudomonas aeruginosa* without an anchoring membrane, *J. Biol. Chem. 272* (35), 21964−21969.
17. Yoneyama, H., Maseda, H., Kamiguchi, H., and Nakae, T. (2000) Function of the membrane fusion protein, MexA, of the MexA, B.-OprM efflux pump in *Pseudomonas aeruginosa* without an anchoring membrane, *J. Biol. Chem. 275* (7), 4628−4634.
18. Kyriacou, S. V., Nowak, M. E., Brownlow, W. J., and Xu, X.-H. N. (2002) Single live cell imaging for real-time monitoring of resistance mechanism in *Pseudomonas aeruginosa*, *J. Biomed. Opt. 7* (4), 576−586.
19. Xu, X.-H. N., Brownlow, W., Huang, S., and Chen, J. (2003) Real-time measurements of single membrane pump efficiency of single living *Pseudomonas aeruginosa* cells using fluorescence microscopy and spectroscopy, *Biochem. Biophys. Res. Commun. 305*, 79−86.
20. Crivellato, E., Candussio, L., Rosati, A. M., Bartoli-Klugmann, F., Mallardi, F., and Decorti, G. (2002) The fluorescent probe Bodipy-FL-verapamil is a substrate for both P-glycoprotein and multidrug resistance-related protein (MRP)-1, *J. Histochem. Cytochem. 50* (5), 731−734, and references therein.
21. Morjani, H., Aouali, N., Belhoussine, R., Veldman, R. J., Levade, T., and Manfait, M. (2001) Elevation of glucosylceramide in multidrug-resistant cancer cells and accumulation in cytoplasmic droplets, *Int. J. Cancer. 94* (2), 157−65, and references therein.
22. Kyriacou, S. V., Brownlow, W., and Xu, X.-H. N. (2004) Nanoparticle optics for direct observation of functions of antimicrobial agents in single live bacterial cells, *Biochemistry 43* (2), 140−147.
23. Xu, X.-H. N., Wan, Q., Kyriacou, S., Brownlow, W., and Nowak, M. (2003) Direct observation of substrate induction of resistance mechanism in *Pseudomonas aeruginosa* using single live cell imaging, *Biochem. Biophys. Res. Commun. 305*, 941−949.
24. Xu, X.-H. N., Chen, J., Jeffers, R., and Kyriacou, S. (2002) Direct measurement of sizes and dynamics of single living membrane transporters using nano-optics, *Nano Lett. 2*, 175−182.
25. Greenwood, D. (1997) Modes of action in antibiotic and chemotherapy, in *Antibiotic and Chemotherapy: Anti-infective Agents and Their Use in Therapy*, (O'Grady, F., Lambert, H. P., Finch, R. G., and Greenwood, D., Eds). 7th ed., pp 10−21, Churchill Livingstone, New York.
26. Lee, P. C., and Meisel, D. (1982) Adsorption and surface-enhanced Raman of dyes on silver and gold sols., *J. Phys. Chem. 86* (17), 3391−3395.
27. Ferraro, M. J., and Wikler, M. A. (2000) NCCLS Methods for Dilution Antimicrobial Susceptibility Tests for Bacteria that Growth Aerobically. 5th ed. Vol. 20 (2), p 44, Ortho-McNeil.
28. Steel, C., Wan, Q., and Xu, X.-H. N. (2004) Single living cell imaging of chromosomes in chloramphenicol-induced filamentous *P. aeruginosa*, *Biochemistry 43*, 175−182.
29. Yoneyama, H., Ocaktan, A., Tsuda, M., and Nakae, T. (1997) The role of Mex-gene products in antibiotic extrusion in *Pseudomonas aeruginosa*, *Biochem. Biophys. Res. Commun. 233*, 611−618.
30. Xu, X.-H. N., and Patel, R. (2004) Nanoparticles for live cell dynamics, in *Encyclopedia of Nanoscience and Nanotechnology*, American Scientific Publishers, Vol. 7, pp 181−192.
31. Xu, X.-H. N., and Patel, R. (2004) Imaging and Assembly of Nanoparticles in Biological Systems, in *Handbook of Nanostructured Biomaterials and Their Applications in Nanobiotechnology*, American Scientific Publishers, Vol. 1 (in press).
32. Xu, X.-H. N., Jeffers, R., Gao, J., and Logan, B. (2001) Novel solution-phase immunoassays for molecular analysis of tumor markers, *Analyst 126*, 1285−1292.
33. Klaus, T., Joerger, R., Olsson, E., and Granqvist, C.-G. (1999) Silver-based crystalline nanoparticles, microbially fabricated, *Proc. Natl. Acad. Sci.* U.S.A. *96* (24), 13611−13614.
34. Mulvaney, P. (1996) Surface plasmon spectroscopy of nanosized metal particles, *Langmuir 12*, 788−800, and references therein.
35. Bohren, C. F. and Huffman, D. R. (1983) *Absorption and Scattering of Light by Small Particles*, pp. 287−380, Wiley, New York, and references therein.
36. Kreibig, U., and Vollmer, M. (1995) *Optical Properties of Metal Clusters*, pp 14−123, Springer, Berlin, and references therein.
37. Mie, G. (1908) Beiträg zur optik trüber medien, speziell kolloidaler metrallösungen. *Ann. Phys. 25*, 377−445.
38. Yoneyama, H., Ocaktan, A., Gotoh, N., Nishino, T., and Nakae, T. (1998) Subunit swapping in the Mex-extrusion pumps in *Pseudomonas aeruginosa*, *Biochem. Biophys. Res. Commun. 244*, 898−902.
39. Li, X. Z., Livermore, D. M., and Nikaido, H. (1994) Role of efflux pump(s) in intrinsic resistance of *Pseudomonas aeruginosa*: resistance to tetracycline, chloramphenicol, and norfloxacin, *Antimicrob. Agents Chemother. 38* (8), 1732−1741.
40. Li. X. Z., Nikaido, H., and Poole, K. (1995) Role of mexA-mexB-oprM in antibiotic efflux in *Pseudomonas aeruginosa*, *Antimicrob. Agents Chemother. 39* (9), 1948−1953.
41. Kyriacou, S. V. (2003) Real-time study of multidrug resistance mechanism in *Pseudomonas aeruginosa* using nanoparticle optics and single live cell imaging, Thesis, Old Dominion University, Norfolk, VA.
42. Haynes, C., and Van Duyne, R. (2001) Nanosphere lithography: a versatile nanofabrication tool for studies of size-dependent nanoparticle optics, *J. Phys. Chem. B 105*, 5599−5611, and references therein.
43. Morgan, A. R., Lee, J. S., Pulleyblank, D. E., Murray, N. L., and Evans, D. H. (1979) Review: ethidium fluorescence assays. part 1. physicochemical studies, *Nucleic Acids Res. 7* (3), 547−569.

BI036231A